Weierstraß-Institut
für Angewandte Analysis und Stochastik

im Forschungsverbund Berlin e.V.

Preprint ISSN 0946 – 8633

Numerical bifurcation analysis of traveling wave model of multisection semiconductor lasers

Mindaugas Radziunas[1]

submitted: 25 Nov 2004

[1] Weierstrass Institute
for Applied Analysis and Stochastics,
Mohrenstraße 39,
D – 10117 Berlin,
Germany
E-Mail: radziuna@wias-berlin.de

No. 985
Berlin 2004

2000 *Mathematics Subject Classification.* 37L65,35B32,78M25,65P30.

Key words and phrases. Numerical bifurcation analysis, traveling wave model, mode approximations, quality of pulsations.

Supported by DFG Research Center MATHEON "Mathematics for key technologies".

Edited by
Weierstraß-Institut für Angewandte Analysis und Stochastik (WIAS)
Mohrenstraße 39
10117 Berlin
Germany

Fax: + 49 30 2044975
E-Mail: preprint@wias-berlin.de
World Wide Web: http://www.wias-berlin.de/

Abstract

Traveling wave equations are used to model the dynamics of multisection semiconductor lasers. To perform a bifurcation analysis of this system of 1-D partial differential equations its low dimensional approximations are constructed and considered. Along this paper this analysis is used for the extensive study of the pulsations in a three section distributed feedback laser. Namely, stability of pulsations, different bifurcation scenaria, tunability of the pulsation frequency and its locking by the frequency of electrical modulation are considered. All these pulsation qualities are highly important when applying lasers in optical communication systems.

1 Introduction

Multisection semiconductor lasers and coupled laser systems are useful devices in different applications. For example, frequency-tunable self-pulsations [1] can be used for clock recovery in optical communication systems.

A deep understanding of these devices is required when designing them for specific functionalities. To describe the dynamical behaviour of such devices models of different complexity can be used. For example, one can use rather complex two or three dimensional partial differential equation (PDE) models originating from Maxwel-Bloch equations [2] as well as simple ordinary differential equation (ODE) or more complex delayed differential equation (DDE) systems based on only few rate equations [3]. Complex models, in general, are more precise and are useful for straightforward integration, but usually they admit only very limited possibilities for analysis. At the same time ODE and DDE models neglect some important physical effects, but when applied to some specific laser structures they still can recover in experiments observable dynamics [4, 5]. In addition, these rather simple models allow a much deeper study of different stationary states of the model [6] as well as the bifurcation mechanisms of dynamical regimes [7].

In the present paper the Traveling Wave (TW) model, given by a hyperbolic system of one dimensional first order PDE's (describing the longitudinal dynamics of counter-propagating optical fields) nonlinearly coupled to a system of ODE's (governing dynamics of polarizations and carrier densities) is considered [8, 9]. As a PDE model, it is already complicated enough and is able to recover spatio-temporal dynamics observed in different configurations of multisection lasers [10, 11, 12, 13]. From the other hand, it is simple enough and, besides straightforward integrations, it allows also a more deep analysis [14, 15]. For simulation and analysis of a hierarchy

of TW models the software *LDSL-tool* (abbreviation for (L)ongitudinal (D)ynamics in multisection (S)emiconductor (L)asers) was developed [16, 17]. It can be used for numerical integration of the model equations as well as for a comprehensive data post-processing and spectral analysis, making it a powerful tool well suited for the study of different dynamical effects. In the present paper, the possibilities of *LDSL-tool* to build and to integrate reduced low dimensional ODE systems, and to validate the precision of approximated systems are discussed. Moreover, it is demonstrated, how a finite dimensional vector field generated by *LDSL-tool* can be applied for further numerical continuation and bifurcation analysis by means of software package AUTO [18].

The Mode Approximation (MA) system of the TW model is based on the projection of the optical field and polarization into a finite dimensional subspace spanned only by a few optical modes depending instantaneously on carrier density [19, 20]. It was proved in [21] that such a center manifold reduction of a PDE system is justified mainly due to the slow variation of the carriers. In [15] a numerical bifurcation analysis of a single and of a two mode approximation systems was presented. In [13, 22] a *qualitative* agreement of the dynamics of the full PDE model and of its its two mode approximation system was shown for some restricted parameter regions. The observed differences were due to simplifications of the TW model used for the construction of the 2MA systems as well as due to neglection of important modes contributing dynamics of the full TW model. In the present paper the number of the selected modes is not restricted to one or two. Here, the identification of the modes participating some stable stationary regime is made after the mode expansion of the simulated optical field in the TW model [17]. It will be shown how a *quantitative* agreement between computed trajectories of the corresponding MA system and the solution of the full TW model admits such a mode selection. Furthermore, this mode selection guarantees *quantitative* agreement between the TW model and the MA systems when continuing stable orbits or their bifurcations in the parameter space.

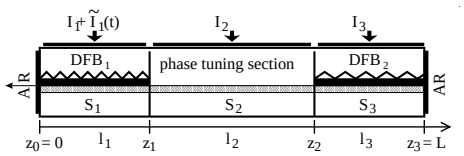

Figure 1: Scheme of a 3 section PhaseCOMB laser.

To illustrate these new possibilities of *LDSL-tool*, a self pulsating three section semiconductor laser is considered. It is completely anti-reflection coated and consists of two distributed feedback (DFB) sections and one phase tuning section integrated in between (see scheme in Fig. 1). It was shown experimentally and theoretically in [11, 16] that by varying some of the laser parameters one can realize nearly harmonic field power pulsations with a ~ 40 GHz frequency required for applications. In [23] it was demonstrated how the pulsation frequency of this Phase Controlled Mode Beating (PhaseCOMB) laser can be locked by an external periodic signal. Hence, such laser could be used for optical clock recovery in optical communication systems. In the present paper, these pulsations are simulated by means of the TW

model and the MA systems. Their stability domain in parameter plane and their locking properties are investigated by a numerical bifurcation analysis tool. Finally, an extensive characterisation of the pulsation quality which is highly important in applications is given by combining all different approaches.

This paper is organized as follows. In Section 2 a full description of the Traveling Wave model is given and the parameters of the considered PhaseCOMB laser are specified. Section 3 introduces the reduced MA systems, and considers the selection of dominant modes. In the following Sections 4 and 5 the numerical bifurcation analysis for nonmodulated and modulated MA systems is performed. After giving an overview of different characteristics of pulsations in Section 6, some conclusions are drawn. In the Appendix explicit expressions of the functions occurring in the MA systems as well as some algorithms used for the construction of these systems are given.

2 A mathematical model of laser dynamics

2.1 Traveling wave model

A multisection laser consisting of m sections S_r, $r = 1, \ldots, m$, with the lengths l_r and the total laser length L is considered (see Fig. 1 where $m = 3$). Along the longitudinal axis of the device counterpropagating complex slowly varying amplitudes of optical fields $E(z,t) = (E^+, E^-)^T$ and polarization functions $p(z,t) = (p^+, p^-)^T$ are governed by the traveling wave equations

$$\begin{aligned} -i\partial_t E^\pm &= v_g \left[(\pm i\partial_z - \beta(n))\, E^\pm - \kappa E^\mp + i\frac{\bar{g}}{2}(E^\pm - p^\pm) \right], \\ -i\partial_t p^\pm &= -i\bar{\gamma}(E^\pm - p^\pm) + \bar{\omega} p^\pm, \\ \beta(n) &\stackrel{def}{=} \delta - i\frac{\alpha}{2} + \frac{(i+\alpha_H)g(n)}{2}, \quad g(n) \stackrel{def}{=} g'(n - n_{tr}). \end{aligned} \tag{1}$$

The fields $E^\pm$ at the laser facets satisfy the reflecting boundary conditions

$$E^+(0,t) = r_0 E^-(0,t), \qquad E^-(L,t) = r_L E^+(L,t). \tag{2}$$

The norm of the field function $|E(z,t)|^2 = |E^+|^2 + |E^-|^2$ represents a local photon density (local power at z divided by the global constant $v_g \sigma \cdot hc/\lambda_0$). The function $n(t) = (n_1, \ldots, n_m)^T$ entering linearly into the gain function $g(n)$ represents sectionally averaged carrier densities within different laser sections. The carrier rate equations governing the densities $n_r(t)$ read as follows:

$$\begin{aligned} \partial_t n_r &= \frac{I_r + \tilde{I}_r(t)}{e l_r \sigma_r} - R_r(n) - \frac{v_{g,r}}{l_r} \Re e\, (E; g(n)E - \bar{g}(E - p))_r\,; \\ R_r(n) &\stackrel{def}{=} A_r n_r + B_r n_r^2 + C_r n_r^3, \qquad r = 1, \ldots, m. \end{aligned} \tag{3}$$

Here, the expression $(\eta;\zeta)_r = \int_{S_r} \eta^* \zeta\, dz$ denotes the usual scalar product of 2-component vector functions within the section S_r. The subscript indices $_r$ are used

to indicate that the parameters, functions or integration borders belong to the section S_r. When these indices are omitted, the considered operations are done for each or for the already indicated section. Superscripts * and ^{T} stand for complex conjugation and transpose, respectively.

Finally, the fields, polarizations and carrier densities at the initial time moment t_0 are denoted as

$$E(z,t_0) = E_{in}(z), \quad p(z,t_0) = p_{in}(z), \quad n(t_0) = n_{in}. \tag{4}$$

Within each section the parameters v_g, κ, δ, α, g', n_{tr} and α_H entering Eq. (1) represent group velocity, real coupling factor between counterpropagating fields, static detuning, internal optical losses, effective differential gain including the transverse confinement factor, transparency carrier density and Henry linewidth enhancement factor, respectively. An inclusion of the polarization equations determins gain dispersion in each laser section fitting it in frequency domain with a Lorentzian function of amplitude $\bar{g} > 0$, full width at half maximum $2\bar{\gamma} < \infty$ and centered at the frequency $\bar{\omega}$ [8]. Sectional parameters I, σ, A, B and C appearing in (3) denote injection current, cross section area of the active zone and three recombination parameters. The function $\tilde{I}(t)$ denotes a possible current modulation and will be discussed in more details in Section 5. Until then it is neglected supposing $\tilde{I}(t) = 0$. Finally, h, c, e, λ_0 and $r_{0,L}$ are Planck constant, speed of light in vacuum, electron charge, central wavelength, and complex facet reflectivity coefficients, respectively.

2.2 Example

To demonstrate the performance of TW model, a self-pulsating PhaseCOMB laser [11, 16, 17] schematically depicted in Fig. 1 and determined by the parameters of Table 1 is considered. For given parameters the considered system has a unique attracting state which can be approached during a sufficiently long transient time interval from arbitrary initial conditions $(E_{in}(z), p_{in}(z), n_{in})$. Such a transition towards a stable orbit during the first 10 ns is shown in Fig. 2.

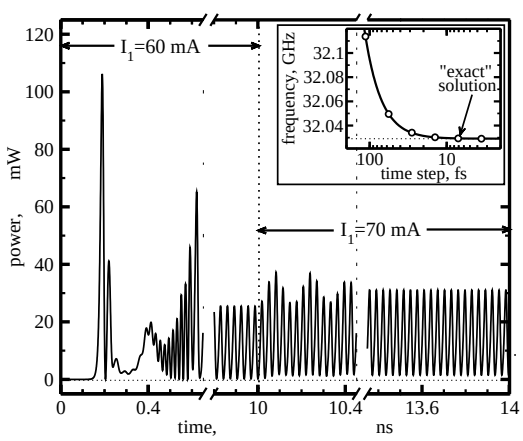

Figure 2: Field output power $|E^-(0,t)|^2$ at left facet. The vertical dotted line at $t = 10$ ns shows where the integration was interrupted and restarted with a new value of the injected current I_1. Insert: convergence of simulated pulsation frequency with decay of grid steps in numerical scheme. Bullets: simulation results. Solid line: fitting by a parabola.

Table 1: Parameters used in simulations.

	explanation	S_1	S_2	S_3	units
c_0/v_g	group velocity factor	3.4	3.4	3.4	
l	length of section	250	400	250	μm
κ	coupling coefficient	130	0	130	cm^{-1}
α	internal absorption	25	20	25	cm^{-1}
g'	effective differential gain	7	0	7	$10^{-17}\mathrm{cm}^2$
δ	static detuning	300	-30	-90	cm^{-1}
α_H	Henry factor	-4		-4	
$\bar{g}$	Lorentzian gain amplitude	200	0	200	cm^{-1}
$\bar{\omega}$	gain peak detuning	0		0	ps^{-1}
$2\bar{\gamma}$	FWHM of gain curve	50		50	ps^{-1}
I	current injection	70		70	mA
σ	cross-section area of AZ	0.45		0.45	$\mu\mathrm{m}^2$
n_{tr}	transparency carrier density	1		1	$10^{18}\mathrm{cm}^{-3}$
A	inverse carrier life time	0.3		0.3	ps^{-1}
B	bimolecular recombination	1		1	$10^{-10}\mathrm{cm}^3/\mathrm{s}$
C	Auger recombination	1		1	$10^{-28}\mathrm{cm}^6/\mathrm{s}$
λ_0	central wavelength		1.57		μm
r_0, r_L	facet reflectivity coefficient		0		

The consequent simulations of the model equations after a slight change of initial parameters are performed starting from the new distributions E_{in}, p_{in} and n_{in} determined by the last moment of the previous simulation. Such selection of initial conditions allows to stay close to the same attractor and to follow its changes in the parameter space. In the given example, at $t = 10$ ns the value of the parameter I_1 was changed and a new simulation was started. Fig. 2 shows that only a short 4 ns transient time is needed to reach again the slightly modified initially close located attractor.

The simulations of the TW model were performed by means of second order precision finite difference (FD) schemes of predictor-corrector type approximating the optical fields $E(z,t)$ along the characteristic lines $z \pm v_g t = const$ [17]. The expected quadratic convergence could be observed with a decay of the grid steps (see, e.g., a quadratic convergence of pulsation frequency as indicated in the insert of Fig. 2). Unfortunately, with decaying grid steps the computation time is quadratically increasing. To perform simulations in reasonable time the temporal grid step is fixed at 7.08333 fs, and simulated solutions are supposed to be the "exact" solutions of the TW model (see indication in the insert of Fig. 2). This exact solution will be used to test the precision of another approach for simulation and analysis of the TW model, what will be discussed in the following section.

3 Reduction of the TW model

In this section the TW model (1,2,3,4) will be reduced to a system of ODE's. The dimension of this system needed to get a good approximation of the initial model will be discussed.

3.1 Mode approximation systems

The equations (1) for the field and the polarization functions can be written in operator form giving rise to the following spectral problem:

$$-i\frac{\partial}{\partial t}\begin{pmatrix}E\\p\end{pmatrix} = H(n)\begin{pmatrix}E\\p\end{pmatrix} \quad \Rightarrow \quad (H(n)-\Omega(n))\,\Theta(n,z)=0. \tag{5}$$

Here, the n-dependent operator H is given by a 4×4 matrix. For any k the k-th eigenfunction Θ^k is suitably scaled and satisfies the boundary conditions corresponding to Eq. (2) (see Appendix for more details).

It was discussed in [21] that field/polarisation functions are exponentially approaching finite dimensional invariant manifold spanned by a finite number of instantaneous modes, i.e., these functions can be approximated by a finite dimensional sum

$$\begin{pmatrix}E\\p\end{pmatrix}(z,t) \approx \sum_{k=1}^{q} f_k(t)\Theta^k(n,z), \tag{6}$$

where $f(t)=(f_1,\ldots,f_q)^T$ represents the complex amplitudes of q dominant modes. The substitution of this truncated mode expansion of the field and the polarization into Eq. (1,3) implies an approximating ($2q$+m)-dimensional MA system of ordinary differential equations for the complex mode intensity functions $f_k^{(q)}$, $k=1,\ldots,q$, and the real carrier density functions $n_r^{(q)}$, $r=1,\ldots,m$:

$$\begin{aligned}
\dot{f}_k^{(q)} &= i\Omega_k(n^{(q)})f_k^{(q)} + \sum_{l=1}^{q}\left(\sum_{r=1}^{m} K_{k,l}^r(n^{(q)})\dot{n}_r^{(q)}\right)f_l^{(q)};\\
\dot{n}_r^{(q)} &= \frac{I_r+\tilde{I}_r(t)}{el_r\sigma_r} - R_r(n^{(q)}) - \Re e\sum_{k,l=1}^{q} L_{k,l}^r(n^{(q)})f_k^{(q)*}f_l^{(q)};\\
f^{(q)}(t_0) &= f_{in} \stackrel{def}{=} f(t_0), \quad n^{(q)}(t_0)=n_{in}.
\end{aligned} \tag{7}$$

Here, the initial value $f(t_0)$ is obtained when decomposing the initial fields / polarisations from (4) into the modal components by means of formula (18). The superscript indices $^{(q)}$ are used to distinguish mode amplitudes and carrier densities originated by the MA system (7) from the field amplitudes f and the densities n representing solution of the full TW model.

Real and imaginary parts of the functions $\Omega(n)$ indicate an approximate angular frequency and damping of the modal amplitude. For any n (and bifurcation parameters P) the values of $\Omega(n)$ are determined numerically by continuing the corresponding roots of the characteristic equation (16) from the previously known values

with slightly different n (and P). After determining $\Omega(n)$ the functions $K^r_{k,l}(n)$ and $L^r_{k,l}(n)$ together with their derivatives can be expressed by explicit formulas (19) as described in the Appendix.

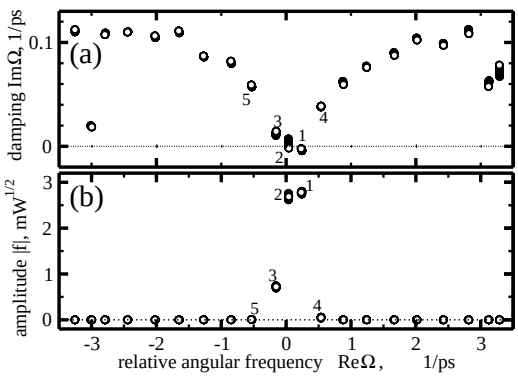

Figure 3: Mode analysis of the pulsating regime of the TW model. Empty and full bullets show the main eigenvalues Ω (panel a) or the modulus of the mode amplitude $|f|$ versus their frequency (panel b) at fixed t or all time moments, respectively.

When building the MA system (7) a few restrictions should be taken into account: First, with the actual change of n and for all considered P each of the main q eigenvalues $\Omega(n)$ should remain separated from any other eigenvalue (see comments on Eq. (17) in Appendix). The unfolding of occurring singularities can be done by selecting another basis of mode expansion (6) close to the mode degeneracy [15, 19]. In the examples of the present paper, nevertheless, such a mode degeneracy does never appear (see, e.g., Fig. 3a where the eigenvalues remain well separated during simulated dynamical regime).

Last but not least, in order to get a satisfactory approximation of exact solutions, among the selected q modes all dominant modes should be present. Such modes in the expansion (6) of any attracting orbit of the TW model should have nonvanishing amplitudes f. To determine all such modes, at the beginning q is assumed to be rather large ($q > 20$ in presented case). Next, following [17] and formula (18) from the Appendix the simulated $E(z,t)$ and $p(z,t)$ can be decomposed into modal components at a few different time instants. The obtained mode amplitudes $|f|$ (located at corresponding modal frequencies $\Re e\Omega$) are represented in Fig. 3b. It is obvious that two-three modes in this case are strongly contributing to the optical fields and should be included when constructing MA systems. The precision of these systems will be discussed in more details below.

3.2 Precision of mode approximations

To estimate the precision of MA systems the comparison of optical fields and carrier densities obtained by integrating different MA systems and the full TW model will be done. For this reason, a trajectory of the TW model starting from distributions $E_{in}(z)$, $p_{in}(z)$ and n_{in} located near the attractor is computed. As it was discussed above, these distributions and formula (18) allow to find an arbitrary number of initial modal amplitudes f_{in}. After choosing the number of modes q, the MA system (7) is integrated numerically.

This integration does not provide the optical fields directly. Nevertheless, being independent on the spatial variable, the solution $(f^{(q)}, n^{(q)})$ of the MA system still allows to reconstruct optical fields or polarizations at any spatial position. For example, the field expansion (6) together with the mode scaling factor $\tilde{c}_0(n, \Omega)$ from (17) imply the following expression of the left facet field output in the MA system:

$$E^{(q)-}(0,t) \stackrel{def}{=} \sum_{k=1}^{q} \tilde{c}_0\left(n^{(q)}(t), \Omega_k(n^{(q)}(t))\right) f_k^{(q)}(t). \tag{8}$$

The power (squared modulus) of this function obtained when integrating 2, 3 and 4 MA systems is depicted by different lines in Fig. 4a. Empty bullets in this figure represent the exact solution of the TW model.

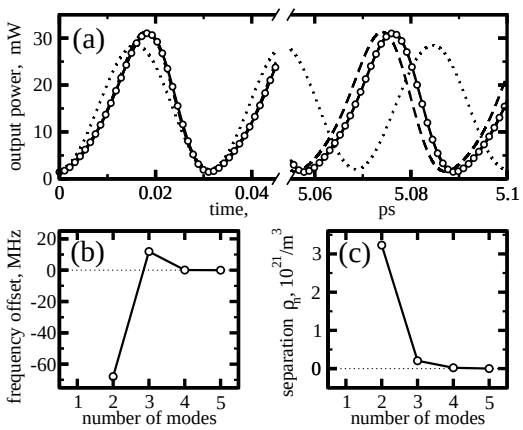

Figure 4: Precision of mode approximations. a: field output power at the left facet. Dotted, dashed and solid lines are due to 2, 3 and 4 mode approximations. Bullets indicate the exact solution. b: difference between the frequency of the pulsations due to MA approach and the pulsation frequency of the exact solution. c: normalized distance ρ_n between the orbits generated by MA systems and the exact orbit.

One can see that a qualitative agreement with the TW model can be realized already with two main modes: 2MA system provides pulsations with a bit smaller symmetric pulses (dotted line in panel a) and slightly different frequency (see panel b). As could be expected from Fig. 3b, only a 3MA system can guarantee a quantitative agreement between slightly asymmetric individual pulses. The small error in the pulsation frequency, nevertheless, still is present. This frequency error is reduced after including the fourth mode as it is indicated in Fig. 3b. The inclusion of further modes makes the integration of the MA system more time consuming without a significant increase of the accuracy.

Besides the output fields (which are mostly interesting in applications and can be measured by engineers) one can also compare the carrier densities which are resolved directly by both the TW model and the MA approaches. The precision of the MA systems can be rapidly estimated when checking the smallness of the maximal separation ρ_n between n-components of different trajectories:

$$\rho_n \stackrel{def}{=} \max_t \left\{ \min_\tau \left\{ \left(\sum_{r=1}^{m} |n_r^{(q)}(t) - n_r(\tau)|^2 \right)^{1/2} \right\} \right\}. \tag{9}$$

In contrast to Fig. 4a, where the pulses of the TW model and the 3MA system were nearly coinciding, this new estimation plotted in panel c shows some small but nonvanishing gap between two compared orbits.

It was shown above how three or four mode approximations are able to recover the orbits of the full TW model with rather good precision. However, one should keep in mind that by tuning some bifurcation parameter the impact of the modes changes and some new mode can become important. In the following sections, where numerical bifurcation analysis will be performed, a 4 MA system will be considered. To ensure the precision of the approximations and the bifurcation analysis, a further comparison of the detected stable orbits of the MA system with the corresponding orbits of the full TW model will be made.

4 Bifurcation analysis

In this section one and two parameter bifurcation diagrams of the TW model and the corresponding MA systems will be presented. The 1-periodic field phase tuning $\varphi = 2L_2\delta_2/2\pi$ and the wavelength detuning $\delta_\lambda = \delta_1 v_{g,1}\lambda_0^2/2\pi c_0$ in the first active DFB section will play the role of bifurcation parameters. Both these parameters, in general, depend on the current injection into the corresponding sections and, therefore, can be controlled in experiments.

4.1 Elimination of rotational invariance

Like the TW model, the MA system is rotationally invariant, i.e., the functions $(f^{(q)}e^{i\phi}, n^{(q)})$ with arbitrary $\phi \in [0, 2\pi]$ represent a family of solutions to (7). This invariance makes no harm when integrating the MA system (7), but can be crucial when performing numerical bifurcation analysis. To avoid such problems, for each $k = 1, \ldots, q$, the real functions

$$y_{2k-2}^{(q)}(t) = \Im m(f_1^{(q)*} f_k^{(q)}), \quad y_{2k-1}^{(q)}(t) = \Re e(f_1^{(q)*} f_k^{(q)}) \tag{10}$$

are introduced so that $y_0^{(q)} = 0$ and the modal amplitude products entering the MA model (7) are given by

$$\left(f_k^{(q)*} f_l^{(q)}\right)(y) = (y_{2k-1}^{(q)} - iy_{2k-2}^{(q)})(y_{2l-1}^{(q)} + iy_{2l-2}^{(q)}) \Big/ y_1^{(q)}.$$

Now the optical field is represented by the $(2q-1)$-dimensional real vector function $y^{(q)}(t) = (y_1^{(q)}, \ldots, y_{2q-1}^{(q)})^T$. After defining the functions

$$\begin{aligned}
\mathcal{L}_r^{(q)}(n, y) &\stackrel{def}{=} \frac{I_r}{el_r\sigma_r} - R_r(n) - \Re e \sum_{k,l=1}^{q} L_{k,l}^r(n) f_k^{(q)*} f_l^{(q)}; \\
\mathcal{K}_k^{(q)}(n, y, \tilde{I}) &\stackrel{def}{=} \sum_{l=1}^{q}\sum_{r=1}^{m} K_{k,l}^r(n) \left(\mathcal{L}_r^{(q)} + \frac{\tilde{I}_r(t)}{el_r\sigma_r}\right) f_1^{(q)*} f_l^{(q)}; \\
\mathcal{M}_k^{(q)}(n, y, \tilde{I}) &\stackrel{def}{=} \left(i(\Omega_k(n) - \Omega_1^*(n)) + \frac{\mathcal{K}_1^{(q)*}}{y_1}\right) f_1^{(q)*} f_k^{(q)} + \mathcal{K}_k^{(q)}
\end{aligned}$$

for $r = 1, \ldots, m$ and $k = 1, \ldots, q$, one can rewrite the resulting $(2q+m-1)$-dimensional MA system without rotational invariance as follows:

$$\begin{aligned}
\dot{y}^{(q)}_{2k-1}(t) &= \Re e \mathcal{M}^{(q)}_k(n^{(q)}, y^{(q)}, \tilde{I}(t)), \qquad k = 1, \ldots, q; \\
\dot{y}^{(q)}_{2k-2}(t) &= \Im m \mathcal{M}^{(q)}_k(n^{(q)}, y^{(q)}, \tilde{I}(t)), \qquad k = 2, \ldots, q; \\
\dot{n}^{(q)}_r(t) &= \mathcal{L}^{(q)}_r(n^{(q)}, y^{(q)}) + \tilde{I}_r(t)/(el_r\sigma_r), \qquad r = 1, \ldots, m; \\
& \quad y^{(q)}(t_0) = y_{in}, \qquad n^{(q)}(t_0) = n_{in}.
\end{aligned} \tag{11}$$

Here, the initial values y_{in} are obtained by applying the transformation (10) to the initial values f_{in} from (7).

The main restriction of this approach is the assumption of nonvanishing first mode, i.e., $y^{(q)}_1(t) = |f^{(q)}_1(t)|^2 \geq \varepsilon > 0$. Only in this case the transformation (10) can be used. In the considered case, this condition holds at least for stable orbits: the stable pulsating regime is determined mainly by two modes whose amplitudes $|f|$ change only slightly in time and remain separated from zero (see the variation of modes 1 and 2 in Fig. 3b). In general, this limitation indicates a necessity of a proper selection and a possible renumbering of the operating modes when continuing the orbits in the parameter space.

4.2 Following orbits in one parameter

In this section bifurcations of the periodic orbits which were computed and discussed in Subsection 3.2 are considered. Fig. 5 represents the continuation of this orbit (indicated by stars at the position $\varphi = B$) if the phase parameter φ changes. It was found that stable periodic orbits of the 3MA (dashed line) and 4MA (solid line) systems loose their stability via a Neimark-Sacker (torus) bifurcation at $\varphi = A$ or a saddle-node (fold) bifurcation at $\varphi = C$. Moreover, in both approximations the orbits are close to each other in a vicinity of $\varphi = A$, are slightly different for $\varphi \in [B, C]$ (see Fig. 5(a)), but possess similar period (frequency) over the considered parameter range (dashed and solid lines coincide in Fig. 5(b)). The analysis of the corresponding stable orbit of the 2MA system (not indicated in Fig. 5) showed again a fold bifurcation at $\varphi \approx C$, but failed totally to locate the torus or some other bifurcation in the vicinity of $\varphi \approx A$.

These discrepancies can be explained after considering the Floquet multipliers of the orbits in different MA systems. Each additional mode in the MA system increases the dimension of the system by two. After neglecting the multiplier 1, the periodic orbits in 4, 3 and 2MA systems can be represented by 8, 6 or 4 multipliers as indicated by different grey shading in Fig. 6.

The stable limit cycle at the position $\varphi = B$ is represented by the inside the unit circle located multipliers (see Fig. 6(b)). At the fold bifurcation one of these multipliers is crossing unit cycle at 1. Since this multiplier (the black bullet on the unit circle in Fig. 6(c)) represents orbits of all three considered MA systems, we have observed the fold bifurcation in all cases. At the phase $\varphi = A$ a pair of complex

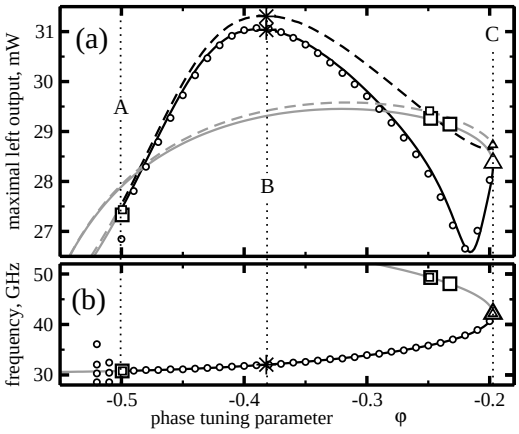

Figure 5: Path following of the periodic orbit. a: maximal output at the left facet. b: frequency of pulsations. Solid, dashed lines and empty bullets are due to 4MA, 3MA and full TW model, respectively. Black and grey lines show stable and unstable orbits in MA systems. Squares and triangles represent torus and fold bifurcations, respectively. The stars at the $\varphi = B$ indicate the orbits considered in Fig. 4.

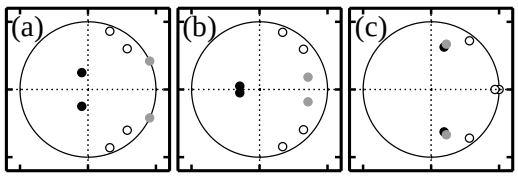

Figure 6: Computed Floquet multipliers of the stable limit cycle at phases A, B and C as shown in Fig. 5. Orbits of 4, 3 and 2MA systems are presented by all, empty and grey, and only empty bullets, respectively.

conjugated multipliers (grey bullets in Fig. 6(a)) are crossing the unit cycle. In this case the multipliers represent only the orbits of the 3MA and 4MA systems, where torus bifurcation was detected. In the 2MA system the multipliers (empty bullets) are remaining inside the unit cycle, and the corresponding orbit remains stable. Similarly, the absence of a pair of multipliers in the 3MA system did allow to locate only one torus bifurcation of the unstable orbit branch within $\varphi \in [B, C]$, while the corresponding orbit of the 4MA system here undergoes two consequent bifurcations (see single small square and two large squares in 3MA and 4MA cases, respectively). This failure in location of the bifurcation shows again the necessity of a proper mode selection.

To check again the precision of the MA systems, simulations of the TW model by changing the bifurcation parameter as it was discussed in Subsection 2.2 were performed. The maxima of the output field power and the frequency of the observed pulsations (determined by the leading components in the Fourier transform of the output power) at each used φ are depicted by open bullets in Fig. 5. As it was predicted by a bifurcation analysis of the 3MA and the 4MA systems, the same type of stable orbit of full TW model was found within the interval $\varphi \in [A, C]$. After its loss of stability at $\varphi = A$, a new attractor was observed possessing at least two different frequencies. The superposition of these frequencies results in multiple peaks in the Fourier spectrum of the output power, some of which are indicated in Fig. 5b for $\varphi < A$. The inspection of the Fourier spectra in order to identify a torus bifurcation is, may be, not very precise, but it is easy accessible in experiments [13]. Finally, the loss of stability of the periodic orbit for $\varphi > C$ in simulations implies a fast transition of the trajectories to some new far away in the phase space located

attractors. Such a behaviour is typical after fold bifurcation where a pair of orbits annihilate each other.

It was demonstrated in Fig. 5 and discussed above that the 4MA as well as the 3MA systems were properly predicting bifurcations of the full TW model, but only orbits of 4MA system were able to be in a perfect qualitative agreement with the exact orbits of the full model. Thus, only 4MA systems will be considered below, where the two parameter bifurcation analysis will be performed.

4.3 Two parameter bifurcation diagram

The continuation of the codimension 1 bifurcations of stable orbits discussed above in the two parameter plane is summarized in Fig. 7. The inspection of the Floquet multipliers of the orbits along the computed bifurcation curves allows to find the stability domain of the orbit discussed in Figs. 4 and 5. . The borders of this domain in Fig. 7 are indicated by black dashed and black solid lines corresponding to the fold and to the torus bifurcations, respectively.

The continuation of the bifurcation branches in two parameters allows to locate codimension 2 bifurcations, some of which are indicated by different symbols in the same figure (see, e.g., the insert of the figure where the enlarged situation in the vicinity of a cusp and 1:1 strong resonance is given). As it was noticed in [24, 25] these points are highly important and acting as "organizing centers" for nearby in the parameter plane located bifurcation diagrams.

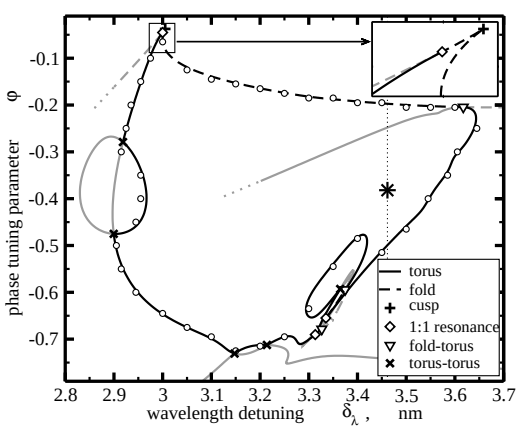

Figure 7: Two parameter bifurcation analysis of the 4MA system. Empty bullets show bifurcations of stable orbit observed in the simulation of the TW model. Black lines and symbols indicate bifurcations of stable orbits. The vertical dotted line and the star on it denote conditions considered in Figs. 5 and 4, respectively.

Together with the bifurcation analysis of the 4MA system simulations of the full TW model were also performed. Like in the example of Fig. 5, by fixing one of the bifurcation parameters and tuning the other one, the bifurcation of periodic orbits was detected. The approximate position of these bifurcations are represented by empty bullets in Fig. 7. The perfect agreement in locating the bifurcations of the stable orbits by means of these two different approaches confirms once more the precision of the MA system based on the initially selected four modes.

Different from the direct integration of the TW model or the MA systems, where only stable orbits are accessible, a numerical bifurcation analysis tool [18] allows to

trace the codimension 1 bifurcations in a parameter plane even though no stable orbits are originating by these bifurcations. Some parts of these "unstable bifurcation" branches are given by grey lines in Fig. 7. Dotted end of such branch indicates either a further loss of stability of the involved orbits or a violation of the nonvanishing main mode condition implied by the MA system (11). Due to this reason and due to the existence of more complicated orbits in our system, which can not be analysed with numerical bifurcation analysis tools (e.g., trajectories on tori), the bifurcation diagram is incomplete. Note also that a large number of unstable orbits (and their bifurcations) of the infinite dimensional TW model was already neglected when projecting this model into the finite dimensional subspace spanned by only a few optical modes. From the other hand, the aim of this paper is not a construction and discussion of the full bifurcation scenario, but a demonstration that bifurcation analysis tools can be applied to our original TW model and can be used to understand bifurcations and some for applications important properties of the in simulations and experiments observable stable orbits. One of such properties, the ability of stable pulsations to be locked by electrical modulation, will be discussed in the next section.

5 Modulation of electrical injection

Let us assume now that the current modulation function $\tilde{I}(t)$ in one of the sections is periodic and nonvanishing. For simplicity, consider a sinusoidal modulation which, following suggestions of [18], can be uniquely described by a pair of real autonomous ODE's with properly selected initial conditions:

$$\begin{aligned} \tilde{I}_r(t) &= \begin{cases} \frac{I_M}{2}\sin(2\pi f_M(t-t_0)) = \frac{I_M}{2}x_1(t), & if \quad r=1 \\ 0, & if \quad r \neq 1 \end{cases}, \\ \dot{x}_1 &= 2\pi f_M x_2 - \Lambda(x_1^2+x_2^2-1)x_1 \qquad x_1(t_0)=0, \\ \dot{x}_2 &= -2\pi f_M x_1 - \Lambda(x_1^2+x_2^2-1)x_2 \qquad x_2(t_0)=1. \end{aligned} \tag{12}$$

The modulation amplitude I_M and the frequency f_M will be considered as bifurcation parameters. The positive constant Λ guarantees the uniqueness of the attracting periodic orbit in the autonomous system (12) and is needed for the stability of computations. Finally, the initial conditions at $t = t_0$ guarantee the validity of relation between $\tilde{I}(t)$ and x_1 given in the first line of Eq. (12) for all time moments. Taking into account these expressions the equations (11, 12) are an autonomous system of ODE's which can be again analysed by means of bifurcation analysis tool AUTO [18].

5.1 Forced locking

Without current modulation ($I_M = 0$) both systems (11) and (12) are decoupled and, independently from each other, possess attracting orbits. The superposition of

these orbits is an invariant two-dimensional torus which attracts all trajectories of the full system (11, 12).

Assuming nonvanishing modulation (e.g., by taking $I_M = 5$ mA as it is done in most of the examples below) two oscillators are unidirectionally coupled. If the separation between the frequency f_N of the stable orbit in the noncoupled system (11) and the modulation frequency f_M remains sufficiently large, then the two systems are coupled only weakly implying again a dynamics on the stable invariant tori. Such behaviour of the coupled MA system (11, 12) as well as of the full TW model (1) with periodic forcing (12) is represented by the Poincaré map iterations which are moving around the attracting invariant closed curve (see left insert of Fig. 8(a)). The high concentration of the iteration points at the right lower part of this curve is due to the coupling of both oscillators and indicates the location where a stable and a saddle periodic orbits of the coupled system will appear.

When the frequency offset $|f_N - f_M|$ becomes small enough, then the coupled system possesses stable and a saddle type periodic orbits. These orbits are fixed points of the Poincaré map (full and empty bullets in right insert of Fig. 8(a)). Here, they are located again on some closed attracting invariant curve. But, in contrast to the previous case, after approaching this curve all iterations are repelled from the saddle state and are converging towards the stable state.

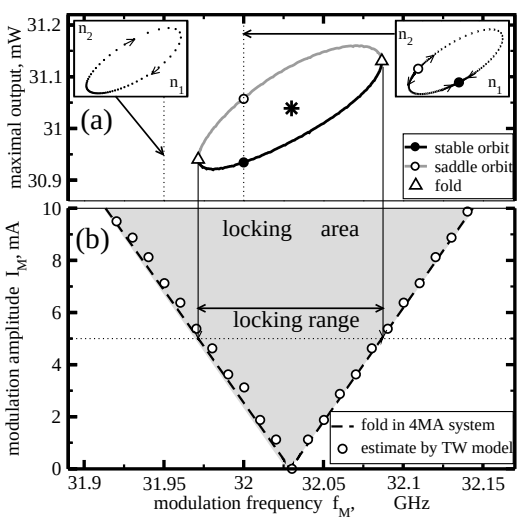

Figure 8: Study of forced locking. a: one parameter bifurcation diagram of the 4MA system with modulated forcing. The star denotes the norm and the frequency f_N of the orbit in the absence of forcing. The inserts represent Poincaré maps for different f_M. Dots indicate the iterations of the map. b: locking area (grey) in a two parameter plane. The borders of the area (dashed lines) are given by folds of limit cycles in the 4MA system or are estimated from full TW model. The dotted line at $I_M = 5$ mA indicates the parameters considered in diagram (a).

The existence of this unique stable state, for which the frequency of the stable periodic orbit of the TW model (1) or of the MA system (11) locks to the frequency f_M is highly important for the applications of pulsating lasers in optical communication systems. For this reason, the study of parameter regions allowing a realization of frequency locking is performed. Fig. 8(a) is due to numerical continuation of the computed stable orbit (black bullet) of the modulated 4MA system when tuning the modulation frequency f_M. Within some frequency interval this orbit remains stable

(black line in this diagram), until it losses the stability in a fold bifurcation, where it collides with a saddle orbit (grey line) and disappears.

In the next step the two fold bifurcations (empty triangles in Fig. 8(a)) of the periodic orbit are traced in the modulation amplitude I_M / frequency f_M plane. These two bifurcation lines (dashed lines in Fig. 8(b)) come together at $I_M = 0$ and $f_M = f_N$. In the given case these lines determine the borders of the *locking* region, where a stable periodic orbit of the coupled system (11,12) can be found. In the sequel the width $\mathcal{R}$ of the locking region at $I_M = 5$ mA is called the *locking range* and is considered as an important characteristic of the periodic orbits.

To estimate the precision of the modulated 4MA system the simulations of the full TW model were performed again. To determine the modus of the operation, the Poincaré map iterations were inspected. The approximate parameter values, where the stable fixed point (full bullet in the right insert of Fig. 8(a)) appears or vanishes were depicted by empty bullets in Fig. 8(b). The small deviation of these bullets from the fold bifurcation lines of the MA system are mainly due to finite steps when tuning the parameters as well as due to the infinite transient times needed to distinguish the iterations of the map at the saddle-node bifurcation.

A nearly linear rise of the bifurcation curves from the origin $(I_M, f_M) = (0, f_N)$ indicates also a small forcing regime. In general, it can be studied by asymptotic methods allowing a rather fast linear estimation of the locking region by finding the slopes of the fold bifurcation lines at the origin. From the other hand, one can also rapidly estimate the locking area by a linear interpolation using the positions (frequencies) of the fold bifurcations at nonvanishing I_M (e.g., frequencies f_M of the triangles in Fig. 8(a)) and the frequency f_N of the periodic orbit in the nonmodulated system. In this case the continuation of the fold bifurcations in f_M and, e.g., φ plane together with the already known dependence $f_N = f_N(\varphi)$ (see Fig. 5(b)) allow a fast estimation of the locking range dependence on the parameter φ.

5.2 Locking of orbits at different phases φ

After fixing the modulation amplitude, the continuation of folds in the (f_M, φ) plane was performed and represented in Fig. 9. To distinguish both fold lines f_1 and f_2, whose frequencies f_M are changing over more than 10 GHz range (see Fig. 5(b) for corresponding frequency tuning of the periodic orbits in the nonmodulated system) the frequency offset $f_M - f_N$ is used for y-axis in panel (a) of this figure. It was checked that for the considered parameter range both fold lines in this diagram give the borders of the region where a stable periodic orbit of the periodically forced MA system exists. Thus, the separation of the fold lines gives an immediate overview on the locking range $\mathcal{R}$ of the pulsations: this range significantly increases near the fold bifurcation of the orbit in the nonmodulated system at $\varphi \approx -0.2$.

Assume that the diagram is a projection of the three dimensional "tube" into a two dimensional parameter plane, where the projection direction was corresponding to

some norm of the orbit (e.g., the maxima of the field output at the left facet, as considered in Fig. 5(a)). The intersection of this "tube" with the fixed φ plane at the positions indicated by stars in Fig. 9(a) was already represented in Fig. 8(a). That is, the front side of the "tube" corresponds to the stable periodic orbit, while the back side represents the saddle type periodic orbit.

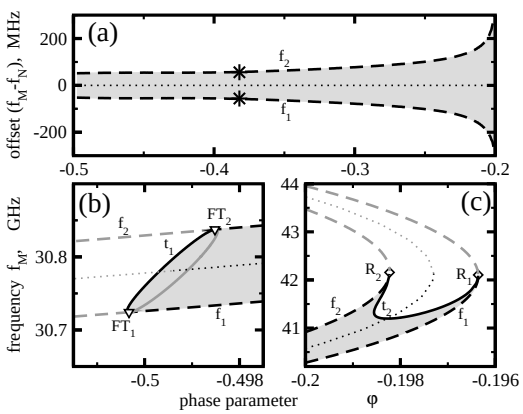

Figure 9: Two parameter bifurcation diagram of the 4MA system along the stable branch of in Fig. 5 shown periodic orbits (a) and nearby φ, where their stability was lost (b,c). The y-axis in (a) represents the frequency offset. Grey shading: areas, where stable orbit exists. Dotted lines: frequency of orbits in the nonmodulated system. Stars: folds considered in Fig. 8. Notation of other lines and symbols as in Fig. 7. Modulation amplitude $I_M = 5$ mA.

At the edges of Fig. 9(a), where the stable orbit of the nonmodulated system bifurcates (see Fig. 5) the situation is represented by Figs. 9(b,c). In panel (b) t_1 is a torus bifurcation branch turning around the "tube". When crossing this line from right to left, the dimension of the unstable manifold of the corresponding orbit decreases by two. The points $FT_{1,2}$ denote a fold-torus interaction, where a pair of complex conjugated and a real positive Floquet multiplier are simultaneously crossing the unit circle. The situation in panel (c) is different. Here, t_2 is again a torus bifurcation branch, but in this case it is located only on the front side of the "tube". The codimension 2 points R_1 and R_2 yield the starting and final points of the branch t_2 are strong 1:1 resonances. Here, two Floquet multipliers are simultaneously becoming equal to 1. If going up towards higher frequencies (or down towards lower frequencies) along fold branches one of these multipliers leaves (enters) the unit circle. When going from these resonances along the t_2 branch, a pair of multipliers split, but remain complex conjugated and located on the unit circle. The branch t_2 distinguishes stable orbits at its left/lower side from the orbits with two dimensional unstable manifold at its right/upper side. The periodic orbits on the back side of the "tube" in the considered parameter range have a one dimensional unstable manifold.

As it is shown in Figs. 9(b,c), at the edges of the parameter region, where the stable orbit of the nonmodulated system exists, the locking range $\mathcal{R}$ can be no more identified simply by the separation of the fold bifurcation lines. However, as it can be seen from the scaling of the x-axis in the discussed diagrams this separation is able to represent $\mathcal{R}$ in most of considered cases. The locking range as well as a few other for applications important characteristics of the stable periodic orbits (pulsations) will be summarized in the next section.

6 Quality of pulsations

In this section the power of the new approach combining simulations of the full TW model and the bifurcation analysis of the MA systems is demonstrated. This approach allows to find parameter regions where for applications needed pulsations exist. It explains their origin, specifies their stability and locking properties. It allows also to find regions of multistability, and to find possible pulsation frequency tuning ranges. The summary of all these properties which are highly important for the clock recovery in optical communication systems [1, 23] is made in Fig. 10. Since practical applications deal mainly with the stable, i.e., observable orbits, all "unstable bifurcation" branches (grey lines of Fig. 7) are omitted and only the area of the stable pulsations is discussed.

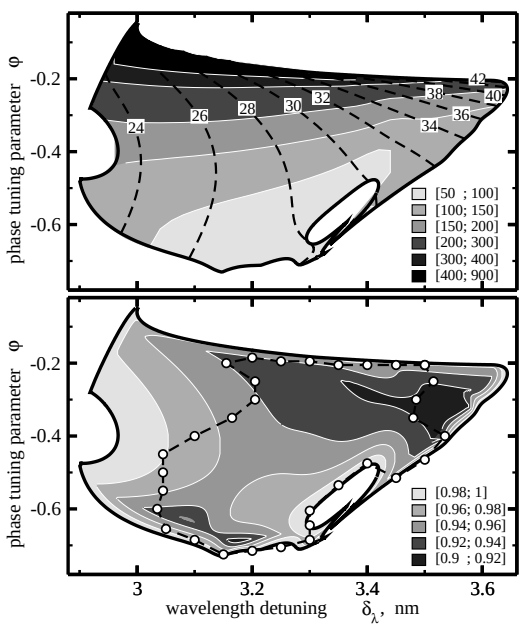

Figure 10: Properties of pulsations. Black dashed curves in (a) are fixed pulsation frequency lines. Different grey shadings show locking range of pulsations at $I_M = 5$ mA in (a) or the stability of pulsations given by the modulus of the maximal Floquet multiplier in (b). These data are due to path following of orbits and the bifurcation analysis of the 4MA system. Empty bullets and dashed line in (b) are due to the inspection of the trajectories in the TW model and indicate an approximate parameter area, where the considered periodic orbit is the unique stable solution.

One of the requirements on the pulsating lasers is a tunability of the pulsation frequency by control parameters. The dashed lines in Fig. 10(a), obtained by tracing fixed period orbits in two parameter plane, indicate an increase of the pulsation frequency with an increase of both considered bifurcation parameters (with decrease of the injected current into the phase section and, e.g., heating of DFB_1 section).

In order to guarantee good locking properties of the pulsations, one needs sufficiently large locking range. To characterize locking of pulsations within in Fig. 10 indicated parameter area, a two parametric bifurcation analysis discussed in Subsection 5.2 and Fig. 9 was performed for series of fixed detuning δ_λ. Different grey shadings in Fig. 10(a) represent the separation between corresponding fold curves which in the interior of the considered area coincide with the locking range $\mathcal{R}$. This diagram shows that the best locking properties one can expect when increasing the phase φ (decreasing injected current into phase section) and operating close to the fold bifurcation of periodic orbits (upper border of the considered area).

The next natural requirement is a better stability of the pulsations. Following the discussion of Subsection 4.2, it can be characterized by the factor $\bar{\mu} = \max_i\{|\mu_i|\}$, where μ_i are the Floquet multipliers of the stable periodic orbit located inside the unit circle at the given parameters (see Fig. 6). The value of this factor for the pulsations within the considered parameter region is represented by different grey shading in Fig. 10(b). The factor $\bar{\mu}$ becomes equal to 1 at the border of the region and is smallest, indicating therefore most stable pulsations at the upper right side of this area.

Finally, it should be also noted that at some of discussed sets of the parameters more than one stable regular or irregular orbit is available. To locate other stable attractors the simulation of the full TW model by tracing stable orbits and approaching considered parameter area from *outside* was made. This continuation was performed until the transition to the originally investigated orbit was observed (see empty bullets in Fig. 10(b)). The transitions which are generated by bifurcations of stable stationary states or periodic orbits can be detected again by a numerical bifurcation analysis tools. Other transitions are due to more complicated phenomena (e.g., boundary crisis of chaotic attractor) and can be only approximately detected by inspection of simulated orbits in the TW model or the MA systems. The parameters between the black solid and dashed lines in Fig. 10(b) support at least two different stable solutions. This multistability should be taken into account when trying to exploit only one of a few existing stable orbits: some perturbation can cause switching of the laser to another, unwanted stable operating regime.

7 Conclusion

In this paper the possibilities of the software *LDSL-tool* to build, to integrate and to analyze finite dimensional systems of ODE's properly approximating the TW model of laser dynamics were presented. It was shown how the combination of bifurcation analysis of MA systems and of integration of the TW model allows to get an extensive characterization of the dynamical regimes of the laser. The characteristics of the pulsating states as frequency tunability, stability, ability to lock to external modulation frequency are highly important for applications in optical communication systems.

Acknowledgments

This work was supported by DFG Research Center MATHEON "Mathematics for key technologies: Modelling, simulation, and optimization of real-world processes". The authot would like to thank K. Schneider for careful reading and discussing the manuscript.

Appendix

All needed functions used in Eq. (7) and (11) except of $\Omega(n)$ have analytic expressions, which are given below in this appendix.

Reformulation of the spectral problem. The eigenfunctions of the spectral problem (5) are four component vector-functions

$$\Theta(n,z) = \begin{pmatrix}\Theta_E\\ \Theta_p\end{pmatrix} = (\Theta_E^+, \Theta_E^-, \Theta_p^+, \Theta_p^-)^T,$$

Taking into account the boundary conditions (2) applicable to the field component Θ_E of the eigenfunction Θ, the spectral problem (5) can be split into two parts:

$$\begin{cases}\partial_z\Theta_E^+(z) = -iD(n,\Omega)\Theta_E^+ - i\kappa\Theta_E^-\\ \partial_z\Theta_E^-(z) = \quad iD(n,\Omega)\Theta_E^- + i\kappa\Theta_E^+\end{cases},$$

$$\Theta_E(n,0)=\tilde{c}_0\begin{pmatrix}r_0\\1\end{pmatrix},\quad \Theta_E(n,L)=\tilde{c}_L\begin{pmatrix}1\\r_L\end{pmatrix},\quad \tilde{c}_{0,L}\in\mathbf{C}; \tag{13}$$

$$\Theta_p(n,z) = \frac{\bar{\gamma}}{\bar{\gamma}+i(\Omega(n)-\bar{\omega})}\,\Theta_E(n,z). \tag{14}$$

System (13) as well as Eq. (14) should be treated separately in each section S_r, where the factor $D(n,\Omega)$ as well as the later used factor $\eta(n,\Omega)$ are, respectively, defined by

$$\begin{aligned} D_r(n,\Omega) &\stackrel{def}{=} \beta_r(n) + \frac{\Omega}{v_{g,r}} - \frac{i\bar{g}_r}{2}\,\frac{i(\Omega-\bar{\omega}_r)}{\bar{\gamma}_r+i(\Omega-\bar{\omega}_r)},\\ \eta_r(n,\Omega) &\stackrel{def}{=} \sqrt{D_r^2-\kappa_r^2}.\end{aligned}$$

Transfer matrices and characteristic function. After fixing n and Ω, Eq. (13) can be easily solved with respect to the function $\Theta(z)$ within each section S_r. The 2×2 transfer matrix

$$M_r(n,\Omega) \stackrel{def}{=} \begin{pmatrix}\cos\eta_r l_r - \frac{iD_r}{\eta_r}\sin\eta_r l_r & -\frac{i\kappa_r}{\eta_r}\sin\eta_r l_r\\ \frac{i\kappa_r}{\eta_r}\sin\eta_r l_r & \cos\eta_r l_r + \frac{iD_r}{\eta_r}\sin\eta_r l_r\end{pmatrix}$$

is used to transmit the function $\Theta_E(n,z)$ from the left edge z_{r-1} to the right edge z_r of the section S_r (see Fig. 1). Taking into account the boundary condition (13) at $z=0$, at any interface z_r of the sections S_r and S_{r+1}, the values of the function Θ_E can be determined by

$$\begin{aligned}\Theta_E(n,z_r) &= \tilde{c}_0\bar{\Theta}_E(n,z_r;\Omega); \qquad \text{where}\\ \bar{\Theta}_E(n,z_r;\Omega) &\stackrel{def}{=} M_r(n,\Omega)\cdots M_1(n,\Omega)\begin{pmatrix}r_0\\1\end{pmatrix}.\end{aligned} \tag{15}$$

In the case Ω is an eigenvalue of the spectral problem, the value of the complex vector $\Theta_E(n,L)$ obtained by means of Equ. (15) should coincide with the boundary

value at $z = L$ as it was defined in Equ. (13). This requirement implies the following definition of the *characteristic* equation

$$\chi(\Omega; n) \stackrel{def}{=} (-r_L, 1)\, M_m(n, \Omega) \cdots M_1(n, \Omega) \binom{r_0}{1} = 0. \tag{16}$$

Thus, for any fixed n, the roots of the complex *characteristic* function $\chi(\Omega; n)$ determine the eigenvalues of the spectral problem (5).

Scaling of the eigenfunctions. To derive the MA systems (7), the orthogonality of Θ and the eigenfunctions

$$\Theta^\dagger = \begin{pmatrix} \Theta_E^\dagger \\ \Theta_p^\dagger \end{pmatrix} = \left(\Theta_E^{-*}, \Theta_E^{+*}, \frac{v_g \bar{g}}{2\bar{\gamma}} \Theta_p^{-*}, \frac{v_g \bar{g}}{2\bar{\gamma}} \Theta_p^{+*} \right)^T$$

of the adjoint problem by means of the scalar product $[\eta; \zeta] = \int_0^L \eta^*(z)\zeta(z)dz$ of four component vector functions η and ζ is employed. In order to have a more simple expression for the functions $K(n)$ and $L(n)$ used in Eq. (7) the eigenfunctions $\Theta(n, z)$ are scaled so that $[\Theta^\dagger; \Theta] = L$. This scaling implies the following expression of the n and Ω dependent complex scaling factor $\tilde{c}_0 = \tilde{c}_0(n, \Omega)$ entering Eq. (13):

$$\tilde{c}_0 = \left(\frac{1}{L} \sum_{r=1}^{m} \left(1 + \frac{v_{g,r} \bar{g}_r \bar{\gamma}_r}{2(\bar{\gamma}_r + i(\Omega - \bar{\omega}_r))^2} \right) \left(\bar{\Theta}_E^\dagger; \bar{\Theta}_E \right)_r \right)^{-\frac{1}{2}}. \tag{17}$$

The formula for the integral expression $(\bar{\Theta}_E^\dagger; \bar{\Theta}_E)_r$ is given below in Eq. (20).

This normalization as well as the derivation of some other formulas below is allowed if only the product $[\bar{\Theta}^\dagger; \bar{\Theta}]$ remains separated from zero. This requirement is violated only in *mode degeneracy* case, i.e., if only related eigenvalue is a multiple root of characteristic equation (16).

Field decomposition into modes. The orthogonality of the functions $\Theta^\dagger$ and Θ is also used when looking for the mode amplitudes $f(t)$ in the decomposition (6) of the computed field $\psi(z, t)$ and the polarization $p(z, t)$ into the modes computed at the actual density $n(t)$:

$$f_k(t) = \frac{1}{L} \left[\Theta^{k\dagger}(n(t), z); \binom{E(z,t)}{p(z,t)} \right]. \tag{18}$$

Definition of the functions entering Eq. (7). The algorithms and formulas giving the functions used in Eq. (7) can be described as follows.

To determine the value of the function $\Omega_k(n)$ with varying n the location of the corresponding root of the characteristic function $\chi(\Omega; n)$ is traced numerically by

means of a homotopy method. The values of $\Omega_k = \Omega_k(n)$, $k = 1, \ldots, q$ are used to define the remaining needed functions $K^r_{k,l}(n)$ and $L^r_{k,l}(n)$ of Eq. (7):

$$K^r_{k,l} \stackrel{def}{=} \begin{cases} \frac{v_{g,r}\tilde{c}_0(n,\Omega_k)\tilde{c}_0(n,\Omega_l)(i+\alpha_{H,r})g'_r}{2L(\Omega_l-\Omega_k)}(\bar{\Theta}^{k\dagger}_E;\bar{\Theta}^l_E)_r, & if \quad k\neq l \\ 0, & if \quad k=l \end{cases};$$

$$L^r_{k,l} \stackrel{def}{=} \frac{v_{g,r}\tilde{c}^*_0(n,\Omega_k)\tilde{c}_0(n,\Omega_l)}{l_r}\Big(g_r(n) - \frac{i\bar{g}_r(\Omega_l-\bar{\omega}_r)}{\bar{\gamma}_r+i(\Omega_l-\bar{\omega}_r)}\Big)(\bar{\Theta}^k_E;\bar{\Theta}^l_E)_r. \tag{19}$$

The integral expressions $(\bar{\Theta}^{k\dagger}_E;\bar{\Theta}^l_E)_r$ and $(\bar{\Theta}^k_E;\bar{\Theta}^l_E)_r$ depend only on the carrier densities n and the numerically computed eigenvalues Ω and are given by

$$\begin{aligned}
(\bar{\Theta}^{k\dagger}_E;\bar{\Theta}^k_E)_r &= \frac{i\kappa_r}{2\eta^2_r(\Omega_k)}\left[(\bar{\Theta}^{k-}_E)^2-(\bar{\Theta}^{k+}_E)^2\right]\Big|^{z_r}_{z_{r-1}} + \\
&\quad + \frac{l_r D^2_r(\Omega_k)}{\eta^2_r(\Omega_k)}\left[2\bar{\Theta}^{k+}_E\bar{\Theta}^{k-}_E + \frac{\kappa_r}{D_r(\Omega_k)}\left((\bar{\Theta}^{k-}_E)^2+(\bar{\Theta}^{k+}_E)^2\right)\right]\Big|_{z_r}; \\
(\bar{\Theta}^{k\dagger}_E;\bar{\Theta}^l_E)_r &= \frac{i}{D_r(\Omega_l)-D_r(\Omega_k)}\left[\bar{\Theta}^{k-}_E\bar{\Theta}^{l+}_E - \bar{\Theta}^{k+}_E\bar{\Theta}^{l-}_E\right]\Big|^{z_r}_{z_{r-1}}, \quad k\neq l; \\
(\bar{\Theta}^k_E;\bar{\Theta}^l_E)_r &= \frac{i}{D_r(\Omega_l)-D^*_r(\Omega_k)}\left[(\bar{\Theta}^{k+}_E)^*\bar{\Theta}^{l+}_E - (\bar{\Theta}^{k-}_E)^*\bar{\Theta}^{l-}_E\right]\Big|^{z_r}_{z_{r-1}}; \\
F\Big|^{z_r}_{z_{r-1}} &\stackrel{def}{=} F(z_r)-F(z_{r-1}), \quad F\Big|_{z_{r-1}} \stackrel{def}{=} F(z_{r-1}).
\end{aligned} \tag{20}$$

The complex factors D_r and η_r are determined in Eq. (15). The values of $\bar{\Theta}^{\pm}_E(n,z)$ at the edges of the sections are given by the analytic formula (15).

Formulas of function derivatives. To find the derivatives of all functions introduced in Eq. (7,11), for all k and r one needs to find the partial n_r and Ω_k derivatives of the functions $\bar{\Theta}^k_E(n,z;\Omega_k)$ computed at the edges of all sections, at the actual value of n and at all corresponding values of Ω_k. At this step all Ω_k are considered as independent variables. Denote any of these derivatives by $\partial_x\bar{\Theta}_E$. Due to the definition of the function $\bar{\Theta}_E$ in (15), the following recurrent formula can be applied:

$$\begin{aligned}
\partial_x\bar{\Theta}_E|_{z_0} &= \binom{0}{0}; \\
\partial_x\bar{\Theta}_E|_{z_r} &= (\partial_x M_r)\bar{\Theta}_E|_{z_{r-1}} + M_r(\partial_x\bar{\Theta}_E)|_{z_{r-1}}, \quad r = 1,\ldots,m.
\end{aligned}$$

Here, the derivatives $\partial_x M_r(n,\Omega_k)$ are obtained by separately differentiating each component of the transfer matrix M_r. Next, all partial ∂_x derivatives of the characteristic function $\chi(\Omega_k;n)$ from (16), the integral expressions (20), the scaling factor $\tilde{c}_0(n,\Omega_k)$ from (17) and the functions $K^r_{k,l}(\Omega_k,\Omega_l,n)$, $L^r_{k,l}(\Omega_k,\Omega_l,n)$ from (19) need to be found.

In the second step the full n_r derivatives of the needed functions taking into account the n dependence of the eigenvalues Ω are derived. In the considered nondegenerate mode case at fixed n all Ω_k are simple roots of the characteristic equation (16), i.e., for each k $\partial_\Omega\chi|_{(\Omega_k,n)}$ remains separated from zero. Thus, due to the implicit function theorem, in a neighbourhood of this fixed n there exist differentiable functions $\Omega_k(n)$ and their n_r derivatives are given by

$$\frac{\partial\Omega_k}{\partial n_r}\Big|_n = -\partial_{n_r}\chi|_{(\Omega_k,n)}\Big/\partial_\Omega\chi|_{(\Omega_k,n)}, \qquad r = 1,\ldots,m.$$

Consequently, the full n_r derivatives of $K^r_{k,l}(n)$ from Eq. (7) now are given by

$$\begin{aligned}\left.\frac{\partial K^r_{k,l}}{\partial n_r}\right|_n &= \partial_{\Omega_k} K^r_{k,l}|_{(\Omega_k,\Omega_l,n)} \left.\frac{\partial \Omega_k}{\partial n_r}\right|_n + \partial_{\Omega_l} K^r_{k,l}|_{(\Omega_k,\Omega_l,n)} \left.\frac{\partial \Omega_l}{\partial n_r}\right|_n + \\ &+ \partial_{n_r} K^r_{k,l}|_{(\Omega_k,\Omega_l,n)}.\end{aligned}$$

Analogously one can find the full n_r derivatives of $L^r_{k,l}(n)$. If needed, in similar manner one can also find partial derivatives with respect to some bifurcation parameter.

References

[1] B. Sartorius, C. Bornholdt, O. Brox et al, *Electron. Lett.*, **34**, pp 1664 (1998)

[2] O. Hess, T. Kuhn, *Prog. Quant. Electr.*, **20(2)**, pp 85–179 (1996)

[3] R. Lang, K. Kobayashi, *IEEE J. Quantum Electron.*, **16**, pp. 347–355, (1980)

[4] S.M. Wieczorek, T.B. Simpson, B. Krauskopf et al,*Phys. Rev. E*, **65**, 045207(R), (2002)

[5] T. Heil, I. Fischer, W. Elsäßer et al, *Phys. Rev. E*, **67**, 066214 (2003)

[6] T. Erneux, A. Gavrielides, K. Green et al, *Phys. Rev. E*, **68**, 066205 (2003)

[7] K. Green, B. Krauskopf, *Phys. Rev. E*, **66**, 016220, (2002)

[8] U. Bandelow, M. Radziunas, J. Sieber et al,*IEEE J. Quantum Electron.*, **37**, pp 183–188 (2001)

[9] J.E. Carroll, J.E.A. Whiteaway, R.G.S. Plumb, *Distributed Feedback Semiconductor Lasers*, (IEE Publishing, 1998)

[10] M. Radziunas, H.-J. Wünsche, B. Sartorius et al,*IEEE J. Quantum Electron.*, **36**, pp 1026–1034 (2000)

[11] M. Möhrle, B. Sartorius, C. Bornholdt et al,*IEEE J. Sel. Top. Quantum Electron.*, **7**, pp 217–223 (2001)

[12] H.-J. Wünshe, O. Brox, M. Radziunas et al, *Phys. Rev. Lett.*, **88**, 023901 (2002)

[13] S. Bauer, O. Brox, J. Kreissl et al, *Phys. Rev. E* , **69**, 016206 (2004)

[14] B. Tromborg, H.E. Lassen, H. Olesen, *IEEE J. Quantum Electron.*, **30**, pp 939 –956 (1994)

[15] J. Sieber, *SIAM J. on Appl. Dyn. Sys.*, **1(2)**, pp 248–270 (2002)

[16] H.-J. Wünsche, M. Radziunas, S. Bauer et al,*IEEE J. Sel. Top. Quantum Electron.*, **9(3)**, pp 857–864 (2003)

[17] M. Radziunas, H.-J. Wünsche, in *Optoelectronic Devices-Advanced Simulation and Analysis*, ed. J. Piprek, (Spinger Verlag, New York 2004)

[18] E. Doedel, R.C. Paffenroth, A.R. Champneys et al,"AUTO2000: Continuation and bifurcation software for ordinary differential equations (with HOMCONT)", *Technical report*, Concordia University (2002)

[19] H. Wenzel, U. Bandelow, H.J. Wünsche, J. Rehberg, *IEEE J. Quantum Electron.*, **32**, pp. 69–79 (1996)

[20] M. Radziunas, H.-J. Wünsche, *SPIE Proc. Ser.*, **4646**, pp 27–37 (2002)

[21] J. Sieber, *Longitudinal Dynamics of Semiconductor Lasers*. PhD Thesis, Faculty of Mathematics and Natural Sciences II, Humboldt-University of Berlin (2001)

[22] J. Sieber, M. Radziunas, K. Schneider, *Mathematical Modelling and Analysis*, **9(1)**, pp 51–66 (2004)

[23] C. Bobbert, J. Kreissl, L. Molle et al:*Electron. Lett.*, **40**, pp 134–135 (2004)

[24] Y.A. Kuznetsov: *Elements of applied bifurcation theory*, (Springer Verlag, New York, 1995)

[25] B. Krauskopf, K.R. Schneider, J. Sieber et al: *Optics Communications*, **215**, pp. 367–379 (2003)